

Comprehensive Synthesis of Magnetic Tornado: Co-spatial Incidence of Chromospheric Swirls and EUV Brightening

HIDETAKA KUNIYOSHI ¹, SOUVIK BOSE ,^{2,3,4,5} AND TAKAAKI YOKOYAMA ⁶

¹*Department of Earth and Planetary Science, The University of Tokyo, 7-3-1 Hongo, Bunkyo-ku, Tokyo, 113-0033, Japan*

²*Lockheed Martin Solar & Astrophysics Laboratory, Palo Alto, CA 94304, USA*

³*Bay Area Environmental Research Institute, NASA Research Park, Moffett Field, CA 94035, USA*

⁴*Institute of Theoretical Astrophysics, University of Oslo, PO Box 1029, Blindern 0315, Oslo, Norway*

⁵*Roseland Centre for Solar Physics, University of Oslo, PO Box 1029, Blindern 0315, Oslo, Norway*

⁶*Astronomical Observatory, Kyoto University, Sakyo-ku, Kyoto, 606-8502, Japan*

ABSTRACT

Magnetic tornadoes, characterized as impulsive Alfvén waves initiated by photospheric vortices in intergranular lanes, are considered efficient energy channels to the corona. Despite their acknowledged importance for solar coronal heating, their observational counterparts from the corona have not been well understood. To address this issue, we use a radiative MHD simulation of a coronal loop with footpoints rooted in the upper convection zone and synthesize the chromospheric and coronal emissions corresponding to a magnetic tornado. Considering SDO/AIA 171 Å and Solar Orbiter/EUI 174 Å channels, our synthesis reveals that the coronal response to magnetic tornadoes can be observed as an EUV brightening of which width is ~ 2 Mm. This brightening is located above the synthesized chromospheric swirl observed in Ca II 8542 Å, Ca II K, and Mg II k lines, which can be detected by instruments such as SST/CRISP, GST/FISS, and IRIS. Considering the height correspondence of the synthesized brightening, magnetic tornadoes can be a mechanism for the small-scale EUV brightenings such as the solar “campfires”. Our findings indicate that coordinated observations encompassing the chromosphere to the corona are indispensable for comprehending the origin of coronal EUV brightenings.

Keywords: Solar coronal heating (1989), Solar chromosphere (1479), Radiative magnetohydrodynamics (2009)

1. INTRODUCTION

The solar coronal heating problem remains a major question in astrophysics. Why do coronal temperatures, exceeding 1,000,000 K, rise hundreds of times higher than photospheric temperatures, which are around $\sim 6,000$ K (Edlén 1943)? While previous studies have revealed that the magnetic field plays a dominant role in the heating (e.g., Parker 1983; Pevtsov et al. 2003), the detailed mechanism is still under investigation (see reviews by Klimchuk 2006; Van Doorsselaere et al. 2020). Of particular interest in this letter is the energy transfer mechanism to the corona, which compensates for the radiative and conductive losses from the corona (Withbroe & Noyes 1977; Díaz Baso et al. 2021).

In the past decades, self-consistent modeling of the energy transfer system has become feasible through the so-called magneto-convection simulations, i.e., radiative magnetohydrodynamic (MHD) simulations, encompass-

ing the upper convection zone, photosphere, chromosphere, and the corona (Leenaarts 2020). These simulations have self-consistently revealed that not only granular-scale ($\sim 1,000$ km) but also smaller-scale (< 200 km) convective motions within intergranular lanes supply a considerable Poynting flux for coronal heating (Rempel 2017; Breu et al. 2022). Magnetic tornadoes, identified as impulsive Alfvén waves originating from photospheric vortex motions within intergranular lanes (Wedemeyer-Böhm et al. 2012; Battaglia et al. 2021), display signatures observed in the photosphere or chromosphere, manifesting as swirling plasma motions (diameter ~ 2 Mm, Shetye et al. 2019; Dakanalis et al. 2022). Magneto-convection simulations focusing on the quiet Sun have indicated that magnetic tornadoes can contribute approximately 50% of the total Poynting flux into the corona (Kuniyoshi et al. 2023; Silva et al. 2024).

Unlike the photospheric and chromospheric observations, the coronal response to magnetic tornadoes has not been well understood. [Wedemeyer-Böhm et al. \(2012\)](#) have detected EUV brightenings over chromospheric swirls using coordinated observations by Atmospheric Imaging Assembly (AIA; [Lemen et al. 2012](#))/Solar Dynamics Observatory (SDO; [Pennell et al. 2012](#)) and Swedish 1-m Solar Telescope (SST; [Scharmer et al. 2003](#))/CRisp Imaging SpectroPolarimeter (CRISP; [Scharmer et al. 2008](#)). On the other hand, [Tziotziou et al. \(2018\)](#) have conducted similar coordinated observation and found an EUV darkening above a chromospheric swirl. To interpret the coronal response accurately, a comprehensive numerical model capable of addressing both chromospheric and coronal signals of magnetic tornadoes is required. Therefore, in this letter, our objective is to synthesize a magnetic tornado within a coronal loop reproduced in a magneto-convection simulation. Unlike our previous simulations, which only considered one half of a loop ([Kuniyoshi et al. 2023, 2024](#)), we now model an entire coronal loop, with the top and bottom boundaries set as the loop footpoints, in accordance with the setup proposed by [Breu et al. \(2022\)](#). This approach mitigates numerical wave reflections from the top boundary at the loop apex, thus averting unrealistic modifications to the coronal energy dissipation system.

2. METHODS

2.1. Simulation Setup

We conduct a three-dimensional magneto-convection simulation using the RAMENS (RAdiation Magnetohydrodynamics Extensive Numerical Solver) code ([Iijima 2016; Iijima & Yokoyama 2017](#)). This code solves the compressible magnetohydrodynamic (MHD) equations with gravity, radiation, and thermal conduction. The basic equations are given in the conservation form as follows:

$$\frac{\partial \rho}{\partial t} + \nabla \cdot (\rho \mathbf{v}) = 0, \quad (1)$$

$$\frac{\partial (\rho \mathbf{v})}{\partial t} + \nabla \cdot \left[\rho \mathbf{v} \mathbf{v} + \left(p + \frac{\mathbf{B}^2}{8\pi} \right) \mathbf{I} - \frac{\mathbf{B} \mathbf{B}}{4\pi} \right] = \rho \mathbf{g}, \quad (2)$$

$$\frac{\partial \mathbf{B}}{\partial t} + \nabla \cdot (\mathbf{v} \mathbf{B} - \mathbf{B} \mathbf{v}) = 0, \quad (3)$$

$$\begin{aligned} \frac{\partial e}{\partial t} + \nabla \cdot \left[\left(e + p + \frac{\mathbf{B}^2}{8\pi} \right) \mathbf{v} - \frac{1}{4\pi} \mathbf{B} (\mathbf{v} \cdot \mathbf{B}) \right] \\ = \rho \mathbf{g} \cdot \mathbf{v} + Q_{\text{cnd}} + Q_{\text{rad}}, \end{aligned} \quad (4)$$

where ρ is the mass density, \mathbf{v} is the gas velocity, \mathbf{B} is the magnetic field, $e = e_{\text{int}} + \rho \mathbf{v}^2/2 + \mathbf{B}^2/8\pi$ is the total

energy density, e_{int} is the internal energy density, p is the gas pressure, \mathbf{g} is the gravitational acceleration, and \mathbf{I} is unit tensor. Q_{cnd} and Q_{rad} denote the heating by thermal conduction and radiation, respectively. Q_{cnd} is Spitzer-type anisotropic thermal conduction. The radiation Q_{rad} is determined through a combination of optically thick and thin components using a bridging law ([Iijima 2016](#)). For optically thick part, we solved the radiative transfer equation under the gray local thermodynamic equilibrium (LTE) assumption. The optically thin part is derived from the radiative loss function retrieved from the CHIANTI atomic database version 7.1 ([Dere et al. 1997; Landi et al. 2012](#)), assuming the coronal abundance. Since the loss function is defined for temperatures $T \geq 10^4$ K, we extrapolate the loss function to the lower temperature range ($\leq 10^4$ K) following the method described in [Goodman & Judge \(2012\)](#). To close the system, the equation of state is calculated under LTE assumption, considering the six most abundant elements in the solar atmosphere (H, He, C, N, O, Ne).

We modified the original RAMENS code to accommodate an entire coronal loop without considering the loop curvature, following the methodology outlined in [Breu et al. \(2022\)](#). The simulation domain spans a horizontal extent of 6 Mm \times 6 Mm in the xy -direction, with a vertical extent of 28 Mm in the z -direction ($-2 \text{ Mm} \leq z \leq 26 \text{ Mm}$). The top ($z = 26 \text{ Mm}$) and bottom ($z = -2 \text{ Mm}$) boundaries correspond to the upper convection zone. The upper convection zones have a depth of 2 Mm below the optical depth τ unity located at $z = 0 \text{ Mm}$ and 24 Mm . Following [Breu et al. \(2022\)](#), we assume a half-circle loop model for the gravitational acceleration as follows

$$\mathbf{g} = -\frac{g \cos \theta}{(1 + h/R_{\text{sun}})^2} \hat{\mathbf{z}}, \quad (5)$$

where $g = 2.74 \times 10^4 \text{ cm s}^{-2}$, $R_{\text{sun}} = 6.96 \times 10^{10} \text{ cm}$, $\theta = z/r$, $h = r \sin \theta$, $r = L_z/\pi$, $L_z = 24 \text{ Mm}$, and $\hat{\mathbf{z}}$ is the unit vector in the z -direction. At the top and bottom boundaries, we impose open boundary conditions for outflows, while fixing the entropy of the inflows through the boundaries to mimic convective energy transport from the deep convection zone (for full details, see [Iijima 2016](#)). In the x - and y -directions, periodic boundary conditions are applied. The grid size is 64 km in the xy -direction and 60 km in the z -direction.

The initial condition in the convection zones is prescribed by Model S ([Christensen-Dalsgaard et al. 1996](#)). Above the surfaces, the initial condition consists of an isothermal stratification permeated by a uniform vertical magnetic field with a strength of 10 G. The convection is allowed to relax after 3 hr of integration. Dur-

ing this period, a thermal conductive flux from the top boundary is imposed to maintain the coronal temperature above 1 MK. Subsequently, this conductive flux is removed, and integration continues for another 1.5 hr to allow the corona to be heated self-consistently by the Poynting flux from both photospheres. We analyze the last 30 min of this period with snapshots taken at intervals of 6 s. Here, we define $t = 0$ s as the start time of this analysis.

2.2. Synthetic Emission

Chromospheric swirls have frequently been observed in Ca II IR and H α by ground-based telescopes such as SST/CRISP (e.g., Shetye et al. 2019; Dakanalis et al. 2022). Additionally, an observation through the Interface Region Imaging Spectrograph (IRIS, De Pontieu et al. 2014) has detected swirls in Mg II line (Park et al. 2016). In this paper, we synthesize Ca II 8542 Å, Ca II K, and Mg II k spectral lines, utilizing the publicly available RH1.5D¹ code (Uitenbroek 2001; Pereira & Uitenbroek 2015). This code can treat optically thick line formation under non-LTE conditions and partial frequency redistribution, which is critical to modelling the chromospheric spectral lines in detail. The 1.5D (column-by-column) treatment of radiation transport is generally valid except at the cores of strong chromospheric lines such as Ca II K and Mg II k where the effects of lateral radiation (3D) transport become important (Sukhorukov & Leenaarts 2017; Bjørgen et al. 2018). However, since the aim of this paper is not a direct comparison of the synthesized observables with actual observations and owing to the substantially high time complexity of 3D non-LTE radiative transfer, the benefits of the 1.5D approach far outweigh its limitations (Pereira & Uitenbroek 2015). Moreover, as shown in Figure 2, the 1.5D approach distinctly reproduces the signature of the swirls in the chromosphere.

For the coronal response, we synthesize the EUV emission as observed in the AIA 171 Å channel. Furthermore, the 174 Å channel of the Extreme Ultraviolet Imager (EUI; Rochus et al. 2020) on board Solar Orbiter (SolO; Müller et al. 2020) is also calculated. The coronal emission is calculated assuming the optically thin approximation under ionization equilibrium, following a methodology similar to that of Chen et al. (2021). The emission I_{corona} is given as:

$$I_{\text{corona}} = \int n_e n_H K(T) ds, \quad (6)$$

where s is the line of sight direction, n_e is electron number density, n_H is hydrogen number density, and $K(T)$ is the contribution function corresponding to the AIA 171 Å and EUI 174 Å channels computed using the FoMo code (Van Doorsselaere et al. 2016). For a direct comparison between the synthesized emission and observations, we consider the pixel sizes of the instruments. The AIA instrument has a spatial resolution of $\approx 1.2''$, while the EUI instrument has $\approx 0.4''$. Following the procedure outlined by Breu et al. (2022), we resample the synthesized emissions by summing up neighboring pixel patches from the numerical model to match the instrumental spatial scale. For simplicity, we did not convolve with the point spread function.

3. RESULTS

3.1. Simulation Overview

Figure 1a and b depict the probability distribution of horizontally averaged temperature T and mass density ρ , denoted as $\langle T \rangle$ and $\langle \rho \rangle$, respectively. It is worth noting that we define the angle brackets $\langle \rangle$ as representing the xy -averaging. $\langle T \rangle$ ranges from 0.5 MK to 0.8 MK, while locally, it exceeds 1 MK. Furthermore, $\langle \rho \rangle$ reveals that chromospheric plasma on the left-hand side extends to higher altitudes ($z = 3\text{--}6$ Mm) compared to the right-hand side. This result arises from a chromospheric jet initiated, which is revisited later.

During the analyzed period, a magnetic tornado is generated by photospheric vortex flows, which is the same triggering mechanism as presented in many previous simulations (Kuniyoshi et al. 2023; Silva et al. 2024). The lifetime of the magnetic tornado is approximately 10 min ($950 \text{ s} \lesssim t \lesssim 1,550 \text{ s}$), corresponding to that of the photospheric vortex, which persists for about one granular turnover time. Figure 1c displays a snapshot of magnetic field lines when the magnetic tornado is produced. It exhibits a coherently twisted feature extending from the left-hand side of the surface ($z = 0$ Mm) to the entire coronal volume. Figure 2d–f illustrates snapshots of the x -component of the magnetic field B_x , vertical Poynting flux S_z (where $S_z = (B_x^2 + B_y^2)v_z/4\pi - (v_x B_x + v_y B_y)B_z/4\pi$), and vertical velocity v_z on the yz -plane at $x = 4.2$ Mm, with the transition region height where $T = 80,000$ K. These quantities clearly depict typical features of magnetic tornadoes. In the region $1 \text{ Mm} < z < 3 \text{ Mm}$, highly twisted B_x with an absolute value reaching over 10 G is observed, extending to the coronal height. Through this region, an amplified vertical Poynting flux S_z exceeding $1 \times 10^7 \text{ erg cm}^{-2} \text{ s}^{-1}$ is channeled into the corona. Additionally, the transition region height increases just above this region to 5 Mm, from which enhanced vertical ve-

¹ <https://github.com/ITA-Solar/rh>

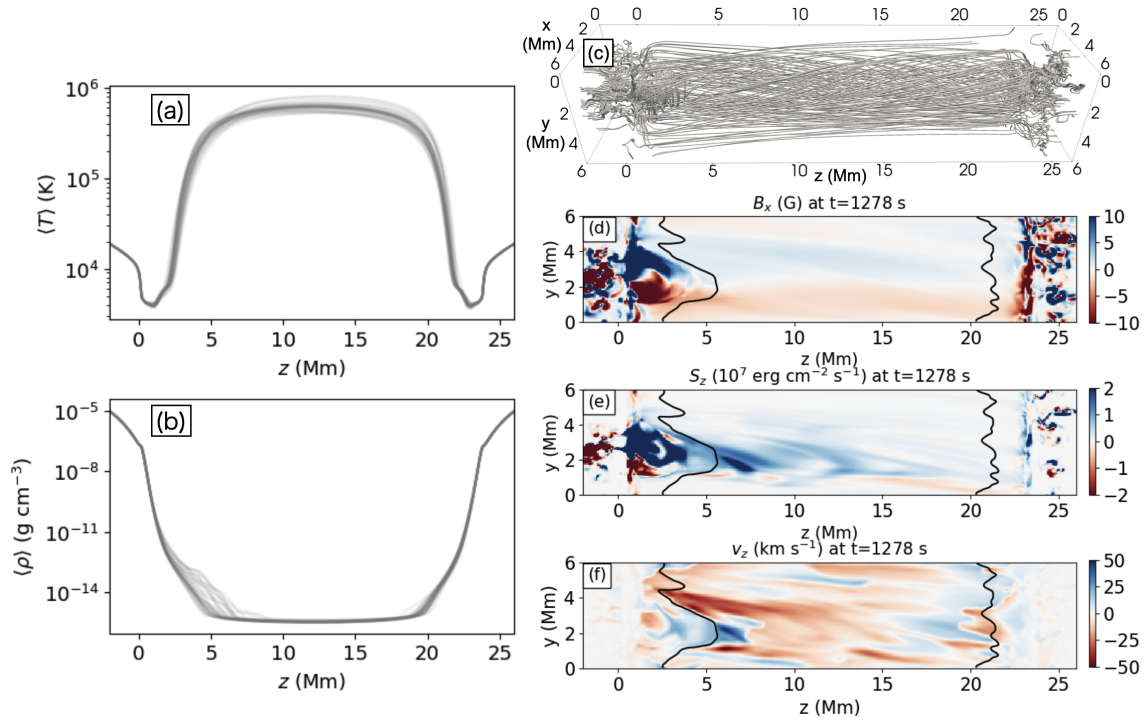


Figure 1. Panel (a) and (b): the probability distributions of the xy -averaged temperature $\langle T \rangle$ and mass density $\langle \rho \rangle$ for t and z . Panel (c)–(f): snapshots ($t = 1,278$ s) of magnetic field lines, B_x , S_z , and v_z on the xz -plane at $x = 4.2$ Mm in the presence of the magnetic tornado. The black contours in panel (d)–(f) indicate the transition region height where $T = 80,000$ K.

locity v_z surpassing 50 km s^{-1} extends into the corona. They are the features of the chromospheric jet driven by the Lorentz force accompanying the magnetic tornado, which is consistent with the previous simulations (Iijima & Yokoyama 2017; Dey et al. 2024).

3.2. Magnetic Tornado Synthesis

In this section, we synthesize the chromospheric and coronal emissions corresponding to the magnetic tornado. The first row of Figure 2 displays the chromospheric synthesis of Ca II 8542 Å, Ca II K, and Mg II k line cores as observed from the negative z -direction at $z = 12$ Mm. These panels and associated animation illustrate that the magnetic tornado can be observed as a rotating swirl-like feature with arc structures, with a diameter of about 3 Mm. The second row shows the $\tau = 1$ formation height corresponding to the wavelength of the images shown in the top row. They reveal that the synthesized swirl originating from the magnetic tornado is formed between $z = 3$ –5 Mm. In Figure 3, horizontal slices of ρ , T , and v_z at corresponding heights $z = 3$ –5 Mm are displayed, with horizontal magnetic field (B_x, B_y) in arrows. These quantities have displayed that the synthesized swirl is characterized by the chromospheric jet with denser and cooler structures than surrounding plasma, upflowing through the twisted magnetic field (see also the corresponding animation).

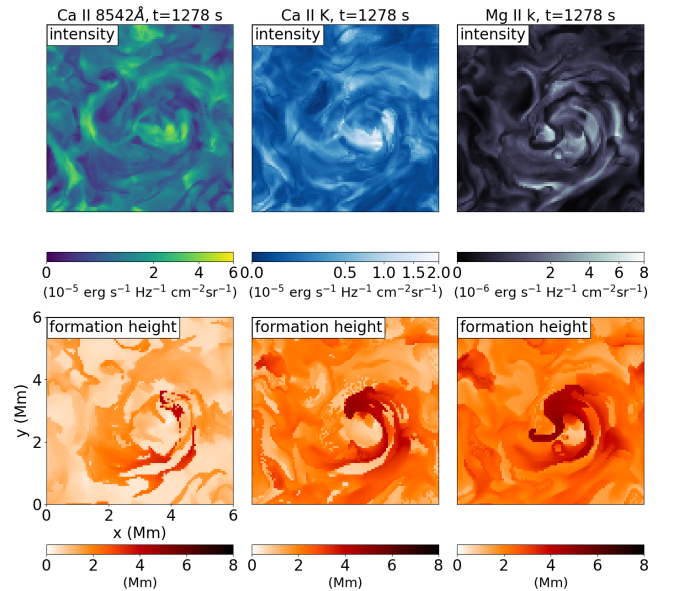


Figure 2. Top row: Snapshots ($t = 1,278$ s) of chromospheric emissions in Ca II 8542 Å, Ca II K, and Mg II k as observed from the coronal apex ($z = 12$ Mm). Bottom row: The formation heights of the emissions. The associated animation shows the temporal evolution over a period from $t = 1,254$ s to $t = 1,350$ s.

Figure 4a–d present the synthesized coronal emission as observed by the SoL/O/EUI 174 Å and SDO/AIA

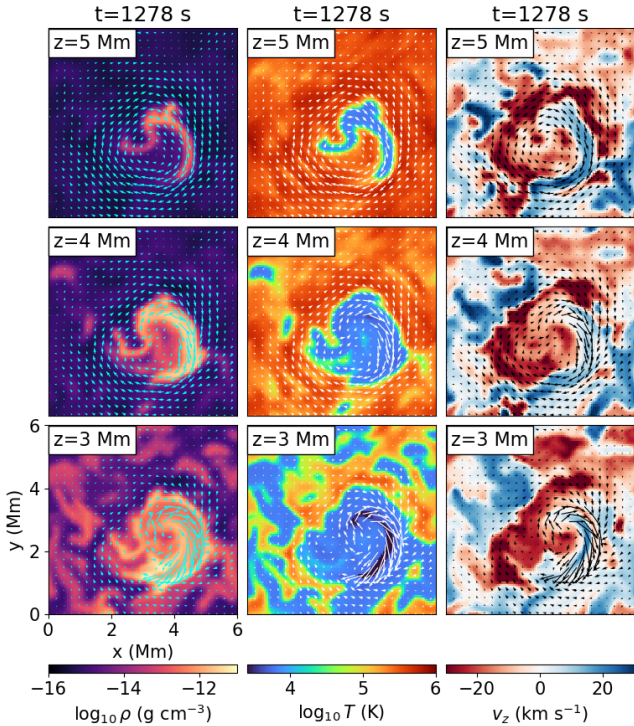


Figure 3. Horizontal slices of ρ , T , and v_z in color with (B_x, B_y) in arrows at $z = 5$ Mm (top row), $z = 4$ Mm (middle row), and $z = 3$ Mm (bottom row) at $t = 1,278$ s. The associated animation shows the temporal evolution over a period from $t = 1,254$ s to $t = 1,350$ s.

171 Å channels from the negative y -direction and positive x -direction at the same time as the chromospheric lines. These panels and associated animations reveal that the EUV brightening occurs within the range of $6 \text{ Mm} \leq z \leq 9 \text{ Mm}$ with a width of approximately 1 Mm, during the period $1,278 \text{ s} \leq t \leq 1,350 \text{ s}$. Although this simulation disregards the curvature of the coronal loop, assuming the coronal loop is semicircular, the corresponding formation altitude from the surface ranges from 5 Mm to 8 Mm. It is important to note that we do not account for EUV absorption by chromospheric materials (such as H I, He I, and He II), as there are no chromospheric jets or prominences generated in front of the coronal brightening along the line of sight of the synthesized emissions.

To analyze the thermal properties of this brightening, Figure 4e–f present the vertical slices of T and ρ at $x = 4.2$ Mm, where the center of the brightening locates. These maps and the corresponding animation show that the brightening is caused by the local enhancement of mass and temperature, resulting from the following processes. First, the transition region height around $y = 1.5\text{--}3$ Mm is lifted due to the chromospheric jet driven by the magnetic tornado (see also Figure 3).

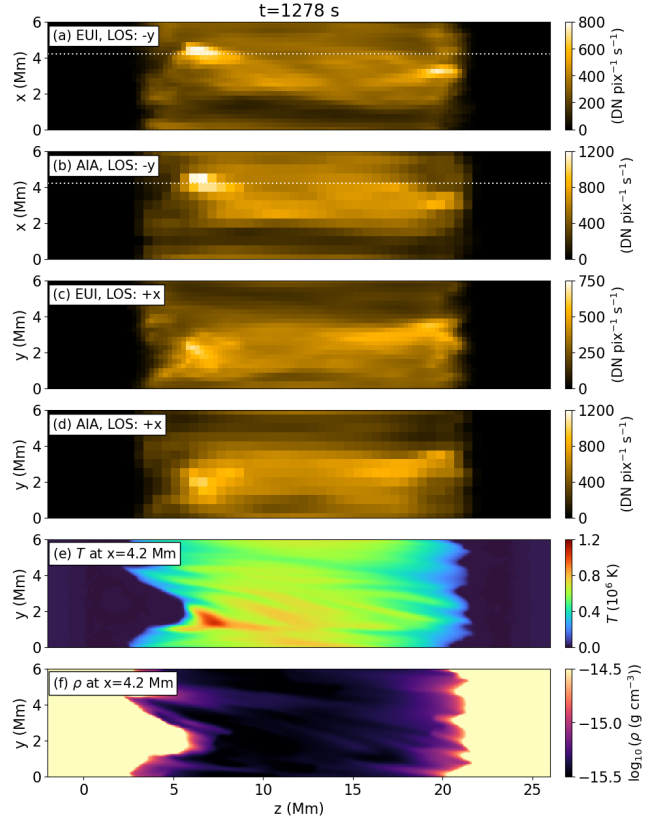


Figure 4. Panel (a)–(d): snapshots ($t = 1,278$ s) of synthesized emissions in the SoLO/EUI 174 Å and SDO/AIA 171 Å channel as seen from the negative y -direction (panel (a) and (b)) and positive x -direction (panel (c) and (d)). Panel (e)–(f): vertical slices of T and ρ through the EUV brightening depicted in panels (a) and (b) ($t = 1,278$ s). These slices are taken at $x = 4.2$ Mm, indicated by the white dashed lines in panels (a) and (b). The corresponding animation shows the temporal evolution over a period from $t = 1,254$ s to $t = 1,350$ s.

This jet then supplies mass to the corona above, which is subsequently heated to over 1 MK. From these results, we can infer that the coronal response to magnetic tornadoes can be observed as local brightenings above chromospheric swirls.

Figure 5a–c display horizontal slices of T , $\alpha = |\nabla \times \mathbf{B}|/B$, and v_z at $z = 7.3$ Mm, where the temperature peak locates at $t = 1,278$ s (see Figure 4e). Additionally, we plot (B_x, B_y) in panel (a) and (v_x, v_y) in panels (b) and (c). The temperature distribution shows that the heating occurs within the twisted magnetic field created by the magnetic tornado. We plot α to confirm whether this heating mechanism is due to magnetic reconnection. α highlights potential reconnection regions, as it is maximized where strong current density coincides with weak magnetic field strength. Around the heated region ($T > 1$ MK), two elongated structures with en-

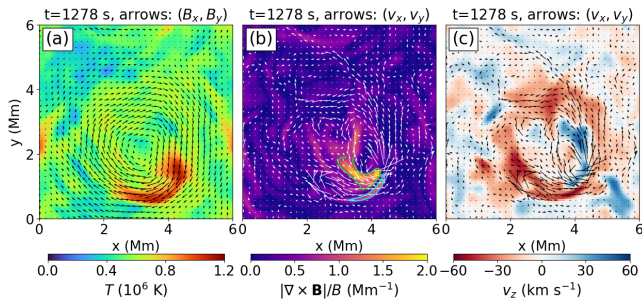


Figure 5. The horizontal slices ($z = 7.3$ Mm) of temperature T , $|\nabla \times \mathbf{B}|/B$ and vertical velocity v_z in color, with horizontal magnetic field (B_x, B_y) or horizontal velocity field (v_x, v_y) in arrows at $t = 1, 278$ s.

hanced α (> 0.8 Mm $^{-1}$) corresponding to current sheets are formed, outlined by cyan (current sheet A) and green lines (current sheet B). Furthermore, the velocity patterns around the current sheets indicate additional signatures of magnetic reconnection. We observe inflow into and bi-directional outflow from the current sheet A. Additionally, an outflow-like velocity pattern in the positive x -direction emerges from current sheet B. However, the other part of the outflow is not visible as it overlaps with the inflow into current sheet A. One part of the outflow from the current sheet A propagates upward ($v_z > 0$) through the background magnetic field, with another part propagating downward ($v_z < 0$). This upflowing heated plasma elucidates the behavior of the EUV brightening, which propagates in the positive z -direction (see the animation associated with Figure 4). These properties suggest that the heating mechanism is the component magnetic reconnection between internally adjacent field lines within the twisted magnetic field.

4. DISCUSSION

Following previous studies (Wedemeyer-Böhm et al. 2012; Tziotziou et al. 2018), our synthesis has illustrated that a magnetic tornado can be observed as a swirl in chromospheric lines. The synthesized swirl in Ca II lines corresponds to previous observations by SST/CRISP, exhibiting a similar diameter of ~ 2 Mm (e.g., Shetye et al. 2019). Our study suggests that chromospheric swirls can also be observed in Mg II k line. This result aligns with previous IRIS observations by Park et al. (2016), which revealed the signature of the chromospheric swirl obtained in a sit-and-stare mode of the Mg II k 2796 Å line. Considering that the diameter of our swirl is sufficiently larger than the spatial resolution of IRIS (0.4" De Pontieu et al. 2014), our synthesis indicates that swirls can be observed in the slit-jaw images (SJIs) in the Mg II k filter.

We have also analyzed the coronal response to the magnetic tornado, as observed in the SolO/EUI 174 Å and SDO/AIA 171 Å channels. From our synthesis, a brightening in both channels is observed above the chromospheric swirl. This result well corresponds to the previous observation by Wedemeyer-Böhm et al. (2012), conducting the coordinated observation by SST/CRISP Ca II 8542 Å line and SDO/AIA 171 Å channel. On the other hand, our result contradicts the observations by Tziotziou et al. (2018), which shows a darkening in AIA 171 Å channel above a chromospheric swirl observed in SST/CRISP Ca II 8542 Å and H α lines. This discrepancy may arise because chromospheric materials such as coronal rains or fibrils positioned over the magnetic tornado, obscure its coronal brightening.

The altitude of the synthesized coronal brightening from the surface ranges from 5 Mm to 8 Mm when we assume our coronal loop to be semi-circular. Interestingly, the lower limit is consistent with the reported formation height of the campfires, at least a portion of which is caused by the coronal EUV brightenings observed by SolO/EUI 174 Å channel (Berghmans et al. 2021). Our results suggest that magnetic tornadoes are likely mechanisms for producing campfires. This aligns with the previous study suggesting that twisted magnetic field structures may play a crucial role in creating at least a portion of campfires (Chen et al. 2021). It should also be noted that the reconnection of low-lying or emerging loops, as well as magnetic flux cancellation, are other promising mechanisms (Berghmans et al. 2021; Panesar et al. 2021). Recent observations propose that the physics behind all the campfires are likely not the same because some have an IRIS counterpart while others do not (Nelson et al. 2023). Therefore, to elucidate the origin of campfires, coordinated observations by ground-based telescopes such as the SST/CRISP or Goode Solar Telescope (GST; Cao et al. 2010)/Fast Imaging Solar Spectrograph (FISS Chae et al. 2013) for the chromosphere and the SolO/EUI for the corona are crucial. If magnetic tornadoes indeed trigger campfires, chromospheric swirls should be observable just below the EUV brightenings.

It is worth noting that spectropolarimetric synthesis of magnetic tornadoes is also performed using the dataset computed by the RAMENS code (Matsumoto et al. 2023). These studies have predicted arc-like linear polarisation signals originating from the highly twisted magnetic field lines, which can be observed by the upcoming polarimetric observations such as SUNRISE III/Sunrise Chromospheric Infrared spectro-Polarimeter (SCIP; Katsukawa et al. 2020), Daniel K. Inouye Solar

Telescope (DKIST; [Rimmele et al. 2020](#)) and European Solar Telescope (EST; [Quintero Noda et al. 2022](#)).

Numerical computations were carried out on the Cray XC50 at the Center for Computational Astrophysics (CfCA), National Astronomical Observatory of Japan. S.B. gratefully acknowledges support from NASA grant 80NSSC20K1272 “Flux emergence and the structure, dynamics, and energetics of the solar atmosphere” and

from NASA contract NNG09FA40C (IRIS). The optically thick synthesis was performed on resources provided by Sigma2 – the National Infrastructure for High Performance Computing and Data Storage in Norway. T.Y. is supported by the JSPS KAKENHI Grant Number JP21H01124, JP20KK0072, and JP21H04492. This work was supported by NAOJ Research Coordination Committee, NINS, Grant Number NAOJ-RCC-2301-0301.

REFERENCES

- Battaglia, A. F., Canivete Cuissa, J. R., Calvo, F., Bossart, A. A., & Steiner, O. 2021, *A&A*, 649, A121, doi: [10.1051/0004-6361/202040110](#)
- Berghmans, D., Auchère, F., Long, D. M., et al. 2021, *A&A*, 656, L4, doi: [10.1051/0004-6361/202140380](#)
- Bjørgen, J. P., Sukhorukov, A. V., Leenaarts, J., et al. 2018, *A&A*, 611, A62, doi: [10.1051/0004-6361/201731926](#)
- Breu, C., Peter, H., Cameron, R., et al. 2022, *A&A*, 658, A45, doi: [10.1051/0004-6361/20214145110.48550/arXiv.2112.11549](#)
- Cao, W., Gorceix, N., Coulter, R., et al. 2010, *Astronomische Nachrichten*, 331, 636, doi: [10.1002/asna.201011390](#)
- Chae, J., Park, H.-M., Ahn, K., et al. 2013, *SoPh*, 288, 1, doi: [10.1007/s11207-012-0147-x](#)
- Chen, Y., Przybylski, D., Peter, H., et al. 2021, *A&A*, 656, L7, doi: [10.1051/0004-6361/202140638](#)
- Christensen-Dalsgaard, J., Dappen, W., Ajukov, S. V., et al. 1996, *Science*, 272, 1286, doi: [10.1126/science.272.5266.1286](#)
- Dakanalis, I., Tsiropoula, G., Tziotziou, K., & Kontogiannis, I. 2022, *A&A*, 663, A94, doi: [10.1051/0004-6361/202243236](#)
- De Pontieu, B., Title, A. M., Lemen, J. R., et al. 2014, *SoPh*, 289, 2733, doi: [10.1007/s11207-014-0485-y](#)
- Dere, K. P., Landi, E., Mason, H. E., Monsignori Fossi, B. C., & Young, P. R. 1997, *A&AS*, 125, 149, doi: [10.1051/aas:1997368](#)
- Dey, S., Chatterjee, P., & Erdelyi, R. 2024, arXiv e-prints, arXiv:2404.16096, doi: [10.48550/arXiv.2404.16096](#)
- Díaz Baso, C. J., de la Cruz Rodríguez, J., & Leenaarts, J. 2021, *A&A*, 647, A188, doi: [10.1051/0004-6361/202040111](#)
- Edlén, B. 1943, *ZA*, 22, 30
- Goodman, M. L., & Judge, P. G. 2012, *ApJ*, 751, 75, doi: [10.1088/0004-637X/751/1/75](#)
- Iijima, H. 2016, PhD thesis, Department of Earth and Planetary Environmental Science, The Univ. of Tokyo
- Iijima, H., & Yokoyama, T. 2017, *ApJ*, 848, 38, doi: [10.3847/1538-4357/aa8ad1](#)
- Katsukawa, Y., del Toro Iniesta, J. C., Solanki, S. K., et al. 2020, in *Society of Photo-Optical Instrumentation Engineers (SPIE) Conference Series*, Vol. 11447, *Ground-based and Airborne Instrumentation for Astronomy VIII*, ed. C. J. Evans, J. J. Bryant, & K. Motohara, 114470Y, doi: [10.1117/12.2561223](#)
- Klimchuk, J. A. 2006, *SoPh*, 234, 41, doi: [10.1007/s11207-006-0055-z](#)
- Kuniyoshi, H., Shoda, M., Iijima, H., & Yokoyama, T. 2023, *ApJ*, 949, 8, doi: [10.3847/1538-4357/acbb8](#)
- Kuniyoshi, H., Shoda, M., Morton, R. J., & Yokoyama, T. 2024, *ApJ*, 960, 118, doi: [10.3847/1538-4357/ad1038](#)
- Landi, E., Del Zanna, G., Young, P. R., Dere, K. P., & Mason, H. E. 2012, *ApJ*, 744, 99, doi: [10.1088/0004-637X/744/2/99](#)
- Leenaarts, J. 2020, *Living Reviews in Solar Physics*, 17, 3, doi: [10.1007/s41116-020-0024-x](#)
- Lemen, J. R., Title, A. M., Akin, D. J., et al. 2012, *SoPh*, 275, 17, doi: [10.1007/s11207-011-9776-8](#)
- Matsumoto, T., Kawabata, Y., Katsukawa, Y., Iijima, H., & Quintero Noda, C. 2023, *MNRAS*, 523, 974, doi: [10.1093/mnras/stad1509](#)
- Müller, D., St. Cyr, O. C., Zouganelis, I., et al. 2020, *A&A*, 642, A1, doi: [10.1051/0004-6361/202038467](#)
- Nelson, C. J., Auchère, F., Aznar Cuadrado, R., et al. 2023, *A&A*, 676, A64, doi: [10.1051/0004-6361/202346144](#)
- Panesar, N. K., Tiwari, S. K., Berghmans, D., et al. 2021, *ApJL*, 921, L20, doi: [10.3847/2041-8213/ac3007](#)
- Park, S. H., Tsiropoula, G., Kontogiannis, I., et al. 2016, *A&A*, 586, A25, doi: [10.1051/0004-6361/201527440](#)
- Parker, E. N. 1983, *ApJ*, 264, 642, doi: [10.1086/160637](#)
- Pereira, T. M. D., & Uitenbroek, H. 2015, *A&A*, 574, A3, doi: [10.1051/0004-6361/201424785](#)
- Pesnell, W. D., Thompson, B. J., & Chamberlin, P. C. 2012, *SoPh*, 275, 3, doi: [10.1007/s11207-011-9841-3](#)

- Pevtsov, A. A., Fisher, G. H., Acton, L. W., et al. 2003, *ApJ*, 598, 1387, doi: [10.1086/378944](https://doi.org/10.1086/378944)
- Quintero Noda, C., Schlichenmaier, R., Bellot Rubio, L. R., et al. 2022, *A&A*, 666, A21, doi: [10.1051/0004-6361/202243867](https://doi.org/10.1051/0004-6361/202243867)
- Rempel, M. 2017, *ApJ*, 834, 10, doi: [10.3847/1538-4357/834/1/10](https://doi.org/10.3847/1538-4357/834/1/10)
- Rimmele, T. R., Warner, M., Keil, S. L., et al. 2020, *SoPh*, 295, 172, doi: [10.1007/s11207-020-01736-7](https://doi.org/10.1007/s11207-020-01736-7)
- Rochus, P., Auchère, F., Berghmans, D., et al. 2020, *A&A*, 642, A8, doi: [10.1051/0004-6361/201936663](https://doi.org/10.1051/0004-6361/201936663)
- Scharmer, G. B., Bjelksjo, K., Korhonen, T. K., Lindberg, B., & Petterson, B. 2003, in *Society of Photo-Optical Instrumentation Engineers (SPIE) Conference Series*, Vol. 4853, *Innovative Telescopes and Instrumentation for Solar Astrophysics*, ed. S. L. Keil & S. V. Avakyan, 341–350, doi: [10.1117/12.460377](https://doi.org/10.1117/12.460377)
- Scharmer, G. B., Narayan, G., Hillberg, T., et al. 2008, *ApJL*, 689, L69, doi: [10.1086/595744](https://doi.org/10.1086/595744)
- Shetye, J., Verwichte, E., Stangalini, M., et al. 2019, *ApJ*, 881, 83, doi: [10.3847/1538-4357/ab2bf9](https://doi.org/10.3847/1538-4357/ab2bf9)
- Silva, S. S. A., Verth, G., Rempel, E. L., et al. 2024, *ApJ*, 963, 10, doi: [10.3847/1538-4357/ad1403](https://doi.org/10.3847/1538-4357/ad1403)
- Sukhorukov, A. V., & Leenaarts, J. 2017, *A&A*, 597, A46, doi: [10.1051/0004-6361/201629086](https://doi.org/10.1051/0004-6361/201629086)
- Tziotziou, K., Tsiropoula, G., Kontogiannis, I., Scullion, E., & Doyle, J. G. 2018, *A&A*, 618, A51, doi: [10.1051/0004-6361/201833101](https://doi.org/10.1051/0004-6361/201833101)
- Uitenbroek, H. 2001, *ApJ*, 557, 389, doi: [10.1086/321659](https://doi.org/10.1086/321659)
- Van Doorselaere, T., Antolin, P., Yuan, D., Reznikova, V., & Magyar, N. 2016, *Frontiers in Astronomy and Space Sciences*, 3, 4, doi: [10.3389/fspas.2016.00004](https://doi.org/10.3389/fspas.2016.00004)
- Van Doorselaere, T., Srivastava, A. K., Antolin, P., et al. 2020, *SSRv*, 216, 140, doi: [10.1007/s11214-020-00770-y](https://doi.org/10.1007/s11214-020-00770-y)
- Wedemeyer-Böhm, S., Scullion, E., Steiner, O., et al. 2012, *Nature*, 486, 505, doi: [10.1038/nature11202](https://doi.org/10.1038/nature11202)
- Withbroe, G. L., & Noyes, R. W. 1977, *ARA&A*, 15, 363, doi: [10.1146/annurev.aa.15.090177.002051](https://doi.org/10.1146/annurev.aa.15.090177.002051)